Characterisation of ordering in A-site deficient perovskite $Ca_{1-x}La_{2x/3}TiO_3$ using STEM / EELS

Mohsen Danaie[1*], Demie Kepaptsoglou[2], Quentin M. Ramasse[2], Colin Ophus[3], Karl R. Whittle[4,5], Sebastian M. Lawson[4], Stella Pedrazzini[1], Neil P. Young[1], Paul A.J. Bagot[1], Philip D. Edmondson[6]

[1]*University of Oxford, Department of Materials, Parks Road, Oxford, OX1 3PH, UK*
[2]*SuperSTEM Laboratory, SciTech Daresbury Campus, Keckwick Ln, Warrington, WA4 4AD, UK*
[3]*National Center for Electron Microscopy, Molecular Foundry, LBNL, 67 Cyclotron Road, Berkeley, CA 94720, USA*
[4]*University of Sheffield, Department of Materials Science & Eng., Immobilisation Science Laboratory, Mappin Street, S1 3JD, UK*
[5]*School of Engineering, University of Liverpool, Brownlow Hill, Liverpool, L69 3GH*
[6]*Materials Science & Technology Division, Oak Ridge National Laboratory, 1 Bethel Valley Road, Oak Ridge, TN 37831, USA*

* Corresponding Author

e-mail: mohsen.danaie@materials.ox.ac.uk, danaie.mohsen@gmail.com

Abstract: The vacancy ordering behaviour of an A-site deficient perovskite system, $Ca_{1-x}La_{2x/3}TiO_3$, was studied using atomic resolution scanning transmission electron microscopy (STEM) in conjunction with electron energy-loss spectroscopy (EELS), with the aim of determining the role of A-site composition changes. At low La content (x = 0.2), adopting Pbnm symmetry, there was no indication of long-range ordering. Domains, with clear boundaries, were observed in bright-field (BF) imaging, but were not immediately visible in the corresponding high-angle annular dark-field (HAADF) image. These boundaries, with the aid of displacement maps from A-site cations in the HAADF signal, are shown to be tilt boundaries. At the La-rich end of the composition (x = 0.9), adopting Cmmm symmetry, long-range ordering of vacancies and La^{3+} ions was observed, with alternating La-rich and La-poor layers on $(001)_p$ planes, creating a double perovskite lattice along the c axis. These highly-ordered domains can be found isolated within a random distribution of vacancies / La^{3+}, or within a large population, encompassing a large volume. In regions with a high number density of double perovskite domains, these highly-ordered domains were separated by twin boundaries, with 90° or 180° lattice rotations across boundaries. The occurrence and characteristics of these ordered structures are discussed and compared with similar perovskite systems.

Keywords: *Perovskite, Ordering, Aberration-corrected electron microscopy, Electron energy-loss spectroscopy*

1 – Introduction

Perovskite structures based on the formulation $Ca_{1-x}La_{2x/3}TiO_3$ have been studied extensively for use across a wide range of possible applications, such as anodes for solid oxide fuel cells (SOFC's),[1] dielectric resonators,[2] high density memory storage devices,[3] as host matrices for inert matrix nuclear fuels and as containment media for high-level nuclear waste forms.[4–6] Understanding the crystallographic ordering at the atomic scale and the nature of defects is essential in order to successfully utilise this class of perovskites across the multitude of applications.

The crystal structure of $CaTiO_3$ at room temperature is known to be orthorhombic adopting Pbnm symmetry, similar to $GdFeO_3$.[7] On heating, there are two phase transitions: firstly to tetragonal I4/mcm at 1523 K and cubic Pm-3m at 1647 K.[7] The high temperature cubic phase adopts the prototypical perovskite structure, ABO_3, with B cations within BO_6 octahedral units and A cations at the centre of a cube with cuboctahedral coordination with O ions, i.e. AO_{12}. In contrast, the structures found at lower temperatures, have lower symmetry, corresponding to changes in BO_6 octahedral tilting, distortions in octahedral spaces, or off-centre B cation.[8] Using Glazer notation,[9] widely used to represent tilts in octahedra within perovskite structures, the high temperature structure is $a^0a^0a^0$, whereas I4/mcm is $a^0a^0c^-$, and Pbnm $a^-a^-c^+$.

As this paper concerns the structural characterisation of $Ca_{1-x}La_{2x/3}TiO_3$, it is instructive to probe the existing literature on the other end member of this compound perovskite as well, i.e. $La_{2/3}TiO_3$. The formation of A-site deficient perovskite in La-Ti-O system, with Ti in +4 oxidation state, was first reported by Kestigian and Ward.[10] [With Ti in purely +3 oxidation state, $LaTiO_3$ is formed with Pbnm symmetry, with a = 5.63 Å, b= 5.61 Å, and c= 7.94 Å.[11,12]] Abe and Uchino were first to synthesise $La_{2/3}TiO_{3-\lambda}$ as a single phase, with the suggested ionic arrangement of $La^{3+}_{2/3}Ti^{4+}_{1-2\lambda}Ti^{3+}_{2\lambda}O^{2-}_{3-\lambda}$ and demonstrating with XRD that with small amount of O deficiency ($\lambda = 0.007$) the {002} line is split into three peaks. This is interpreted as doubling of the unit cell along c-axis, resulting from a more facile formation of the perovskite phase with vacancy ordering on the A-sites.[13] Critical in attracting attention to this system was the report of high ionic conductivity in $Li_{0.34}La_{0.51}TiO_{2.94}$, due to large number of available vacant sites to diffusing Li ions.[14] Other studies report that pure $La_{2/3}TiO_3$ (also written as $La_2Ti_3O_9$) could not be stabilised,[15,16] or have indexed this structure as tetragonal (I4/mmm) with a = b = 3.856 Å, and c = 24.6 Å.[17] The latter structure corresponds to a layered ordering configuration along $[001]_p$ with 2 layers filled and one layer vacant A-sites, hence the relatively large c axis for this unit cell.

Previous structure determinations of $Ca_{1-x}La_{2x/3}TiO_3$ perovskites have used X-ray and neutron diffraction. Vashook et al.[1] examined the phase transitions within the $Ca_{1-x}La_{2x/3}TiO_3$ series using X-ray diffraction, showing that for the Ca-rich composition (x = 0.2) the structure adopted Pbnm symmetry, changing to a body-centred orthorhombic symmetry (Imma) at x = 0.4. At the La-rich composition (x = 0.9) two structures were equally possible, monoclinic (P2/m) and orthorhombic (Cm2m). Vashook et al.[1] highlighted the peculiarity of the La(Ca) cation ordering and the A-site vacancies in $La_{0.6}Ca_{0.1}TiO_3$, which was absent in both $La_{0.13}Ca_{0.8}TiO_3$ and $La_{0.4}Ca_{0.4}TiO_3$. More recently,[18] using synchrotron X-rays, the symmetries in $Ca_{1-x}La_{2x/3}TiO_3$ were identified as Pbnm (x = 0.0 – 0.3), Imma (x = 0.4-0.6), I4/mcm (x = 0.7-0.75), and finally Cmmm for the La-rich extreme case (x = 0.8-0.98). For this La-rich phase an ordered perovskite structure with alternatingly fully and partially (40%) occupied layers of A-site cations was observed. Zhang et al.[19] combined neutron and synchrotron X-ray structural refinements on nominally the same system, showing the following phase stability regions:

i) $0 \leq x \leq 0.5$ - Pbnm symmetry

ii) $0.5 < x < 0.7$ - Ibmm symmetry

iii) $0.7 \leq x < 0.9$ - I4/mcm symmetry

iv) $x \geq 0.9$ - Cmmm, with long range ordering found at x = 0.9

Whilst these techniques provide atomic scale information of both the unit cell and lattice, they are averaged over the entire volume examined. As such, they can be less sensitive to atomic scale segregation or ordering within the lattice. Aberration-corrected scanning transmission electron microscopy (STEM) in conjunction with electron energy-loss spectroscopy (EELS), provides an alternative approach to resolve atomic-scale segregation and / or ordering in such systems.

Table 1 presents an overview of the space groups occurring in the CLTO system across the full-range of composition, using data provided by Zhang et al.[19] The TiO_6 octahedra tilts in each case are shown in the crystal models, also provided in Glazer's notation in the third column.[19,20] In the case of the Cmmm space group, besides the tilt in octahedra, there is significant displacement of the B-site cation (Ti) within the octahedral space (the difference between maximum and minimum Ti-O bond lengths accounts for 9.66%), concurrent with distortions in the TiO_6 octahedral space, i.e. ~5.5 % of the maximum O-O bond length disparity. There are small distortions present in the B-site within the other space groups, but the Ti-O bond length differences are very small (< 0.7%) and, at least in the context of the present study, can be ignored.

In the present study we performed detailed atomic scale characterisation using scanning transmission electron microscopy concurrent with electron energy-loss spectroscopy (STEM / EELS), taking advantage of the different modes of STEM high-resolution imaging, spectroscopy, and through computational electron microscopy. Using this approach, we elucidate the localised characteristics of ordering within the $Ca_{1-x}La_{2x/3}TiO_3$ system, with variation in x, and identify a high number density of various types of tilt boundaries. These atomic scale features are inaccessible in a volume-averaged X-ray or neutron diffraction experiments performed in the past,[19] upon which we are building up the present investigation.

2- Experimental

The $Ca_{1-x}La_{2x/3}TiO_3$ specimens (x = 0.0, 0.1, …0.9) were prepared by solid-state calcination of mixed oxides. Stoichiometric amounts of La_2O_3 (Alfa Aesar 99.99 %), were dried at 1073 K for 24 hours, TiO_2 (Sigma-Aldrich ≥ 99 %) and $CaCO_3$ (Alfa Aesar 99.5 %), were dried at 453 K for 24 hours, prior to weighing, then all were milled with isopropanol in a planetary ball-mill. Once dried, the powders were sieved, pressed into pellets and heated to 1573 K in air for 24 hours, with a ramp rate of 5 $Kmin^{-1}$. Following this they were reground, sieved and pressed once more before sintering at 1673 K in air for a further 48 hours, achieving a relative sample density of > 95 % of the theoretical value, determined via the Archimedes method. The final pellets were ground with silicon carbide and polished to a 1 μm finish with diamond suspension (MatPrep) prior to thermal etching at 1523 K for 2 hours in air. X-ray diffraction patterns were recorded using a STOE STADI P image plate diffractometer with Cu Kα1 (λ = 1.5406Å) beam, at 40 kV, 35 mA. The patterns were collected between 0° and 100° with an integrated step size of 0.03° and an average counting time of 1 s per point. The alignment was checked using an independent silicon calibration run.

Samples for transmission electron microscopy were prepared using both the focused-ion beam (FIB) lift-out technique[21] (Zeiss-NVision 40) and by grinding the pellets into electron-transparent particles, subsequently suspended in high purity chloroform, dispersed onto a gold-supported lacey carbon network (Agar Lacey carbon film, H7 Au) and then dried in air. Samples prepared via FIB lift-out were initially coated with a thin layer of gold for better conductivity. To ensure minimal Ga-beam damage, the TEM lamellae were polished with gradually decreasing beam accelerating voltage and current, with a final cleaning done with a 2 kV Ga beam. All samples were stored under vacuum after preparation.

Space group	Projection along $[001]_p$	Projection along $[100]_p$	Unit Cell Tilt system (Glazer notation)
Pbnm	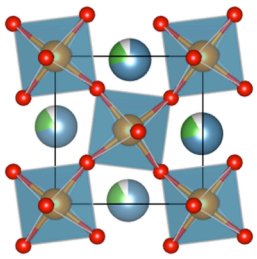	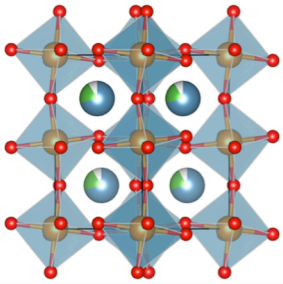	$a = a_p\sqrt{2}$ $b = b_p\sqrt{2}$ $c = 2c_p$ $a^-a^-c^+$
Ibmm	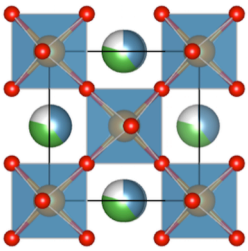	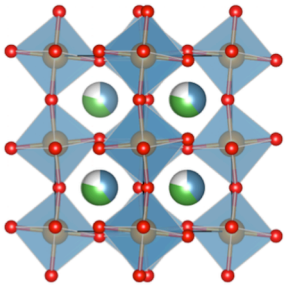	$a = a_p\sqrt{2}$ $b = b_p\sqrt{2}$ $c = 2c_p$ $a^-a^-c^0$
I4/mcm	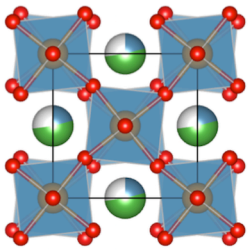	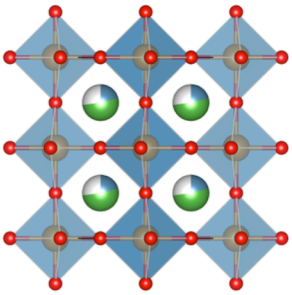	$a = b = a_p\sqrt{2}$ $c = 2c_p$ $a^0a^0c^-$
Cmmm	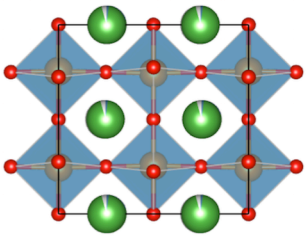	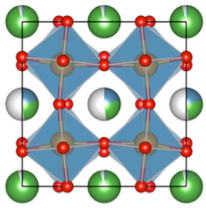	$a = 2a_p$ $b = 2b_p$ $c = 2c_p$ $a^-b^0c^0$

Table 1- Crystal structures of the reported[11] in the CLTO system along the pseudo-cubic directions $[001]_p$ and $[100]_p$. The third column provides the relationships between the pseudo-cubic and actual unit cells and the octahedra tilt system (in Glazer notation). [Colour scheme: Ti orange, O red, Ca blue, and La green]

Preliminary TEM characterisation was performed using a JEOL 2100 microscope, operated at accelerating voltages of 80 kV and at 200kV. The lower voltage was aimed at screening suitable regions for subsequent STEM/EELS analysis. STEM / EELS analysis was performed using a Nion UltraSTEM 100^{TM} dedicated ultrahigh vacuum scanning transmission electron microscope, equipped with a Gatan

Enfina EELS spectrometer (SuperSTEM, Daresbury) operated at 100 kV accelerating voltage, with ~0.3 eV native energy resolution, measured at full-width at half maximum of the zero-loss peak. The effective energy resolution for the experiments was limited by the spectrometer detector point spread function, which is dependent on the dispersion chosen. The probe-forming optics were adjusted to provide a beam of ~100 pA with a convergence semi-angle of 32 mrad, corresponding to a 0.9 Å probe size. The high-angle annular dark-field detector used to record the images had a semi-angular range of 85-190 mrad, while the bright-field detector covered a semi-angular range of 3.4 mrad; annular bright-field (ABF) images were also acquired, with a detector adjusted to cover a semi-angular range of 15-32 mrad. In these settings, a second annular detector can record simultaneously a low-angle annular dark-field (LAADF) signal over a 35-190 mrad semi-angular range. Energy loss spectra were acquired using a collection semi-angle of 36 mrad. High-angle annular dark-field (HAADF) and bright-field (BF) images were acquired simultaneously. The BF signal is largely dominated by phase contrast (similar to high-resolution TEM imaging by reciprocity principle), whereas the HAADF signal is largely due to thermal diffuse scattering, hence incoherent, and sensitive to atomic number (Z).[22] These two imaging signals are complementary in detecting variations in the octahedral tilting (BF[23,24] and ABF[25]) versus the distribution of heavier elements, i.e. Ti, Ca, and La (HAADF). As a rule of thumb, in order for the ADF image to be interpretable as Z-contrast the inner collection angle of the detector has to be around three times the probe half-angle.[26] With the angular values stated as above, this is satisfied for the HAADF signal presented.

For simulation of the selected area diffraction patterns the JEMS software was used.[27] Throughout this paper, unless specified, plane / orientation indices are provided with respect to the pseudo-cubic unit cell, emphasized with the subscript “p”. To perform accurate image analysis on STEM micrographs two techniques were utilized to enhance signal-to-noise ratio: (i) fast (typically 5 μsec per pixel) acquisition of multiple frames, which were then aligned and summed using Digital Micrograph, and (ii) non-linear drift correction using 0° and 90° scan rotation pairs acquired at slower rates (typically 150 μsec per pixel).[28] For a number of drift-corrected datasets, using a peak-finding algorithm implemented in a MATLAB code, where a five-parameter Gaussian function was fitted to the peak positions, mean ‘unit cells’ were constructed by averaging along an axis of interest in the HAADF images. These were then utilised to plot displacement maps of the cations along different zone axes. Multislice STEM image simulations with 8 frozen phonon configurations were performed with custom written Matlab code, using the methods and potentials outlined by E.J. Kirkland.[29] Simulation parameters were set to match the experimental conditions.

3- Results

3-1- X-ray diffraction

X-ray diffraction patterns across the compositional range of the as-prepared $Ca_{1-x}La_{2x/3}TiO_3$ system, are shown in Figure 1. All plots were normalized to the peak intensity for the $\{110\}_p$ pseudo-cubic reflection, the strongest reflection in all cases. It can be seen that the main pseudo-cubic reflections shift towards larger d-spacing values with increasing La content. This can be attributed to the slightly larger size of the La^{3+} ion (electronic structure of La is: [Xe] $5d^1$ $6s^2$, rarely adopting oxidation states other than 3+)[30] compared to the Ca^{2+} (117.2 pm versus 114 pm[31]). This shift agrees with the neutron diffraction analysis performed by Zhang et al.[19] Using X-ray diffraction alone, it is difficult to determine the composition at which the transition from Pbnm ($a^-a^-c^+$) to Ibmm ($a^-a^-c^0$), i.e. the disappearance of the ½{310} peak corresponding to the in-phase c^+ tilt,[32] occurs. Whereas, using neutron diffraction, it is clear this takes place at x = 0.6 CLTO composition.[19]

Given the limitations with X-ray diffraction, it is difficult to definitively ascertain the formation of the Ibmm and the I4/mcm space groups. In contrast, the formation of the Cmmm space group by x = 0.9 is evident in our data. This is highlighted by the splitting of the $\{200\}_p$ peak into a triplet, Figure 1(b), suggesting a transition to orthorhombic symmetry, coupled with the emergence of a peak at $½\{401\}_p$. The tilt system for Cmmm is $a^-b^0c^0$, so we expect to see a reflection at ½{311},[32] as also seen using neutron diffraction.[19] The data here shows the peak at ½{311} strongly present in the Pbnm ($a^-a^-c^+$) space group, but gradually diminishing at higher x values. This is likely to arise from the different scattering parameters for X-rays and neutrons. The peak at ½{401}, given the tilt system of $a^-b^0c^0$ for this space group, would not normally be expected to be associated with octahedral tilting and most likely corresponds to an off-centre Ti position within the octahedron.

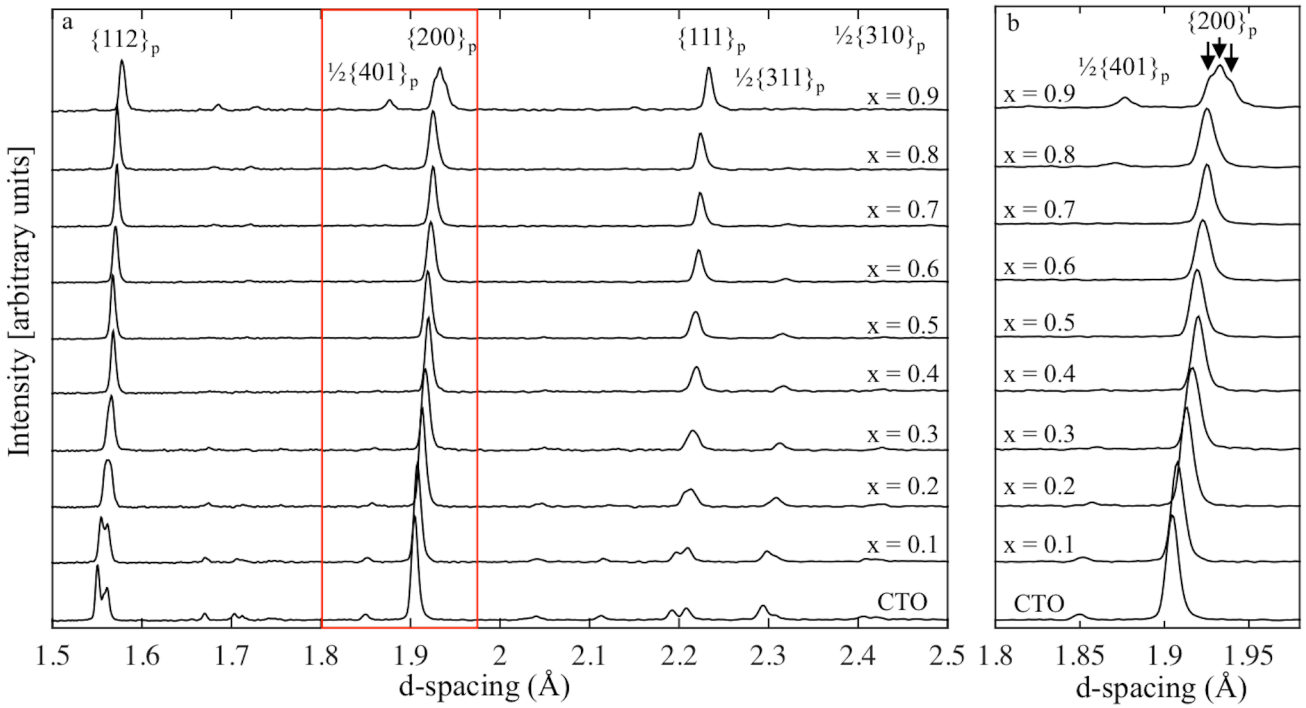

Figure 1- (a) X-ray diffraction data for the complete composition range in the CLTO ($Ca_{1-x}La_{2x/3}TiO_3$) system. Indices are provided with respect to the pseudo-cubic cell. Plot in (b) shows the details of the $\{200\}_p$ peak. Diffractograms are normalized with respect to the $\{110\}_p$ peak intensity and shifted in y-direction for better visibility.

As the presence of the Ibmm and I4/mcm symmetries could not be confirmed by XRD, TEM characterisation was limited to those that could, i.e. Pbnm and Cmmm. Given the narrow stability region for Ibmm and I4/mcm symmetries, it is possible that for compositions x = 0.6 to 0.8 there is a mixture of phases. Hence, we will focus on the extreme cases of La-lean (Pbnm) and La-rich (Cmmm) space groups for electron microscopy characterisation.

3-2- Electron microscopy characterisation- CLTO with low La content (x = 0.1 to 0.5)

Low magnification TEM observations of the low La-content CLTO samples reveal relatively large (> 0.5 μm in size) domains separated with wide defect structures. Figure 2 shows the case for x= 0.1 CLTO using a FIB-prepared sample. A series of selected area diffraction patterns were acquired across the region shown in Figure 2(a), with the numbered circles indicating the regions corresponding to the experimental electron diffraction patterns, presented in Figure 2(b). In pattern 1, there is a good match

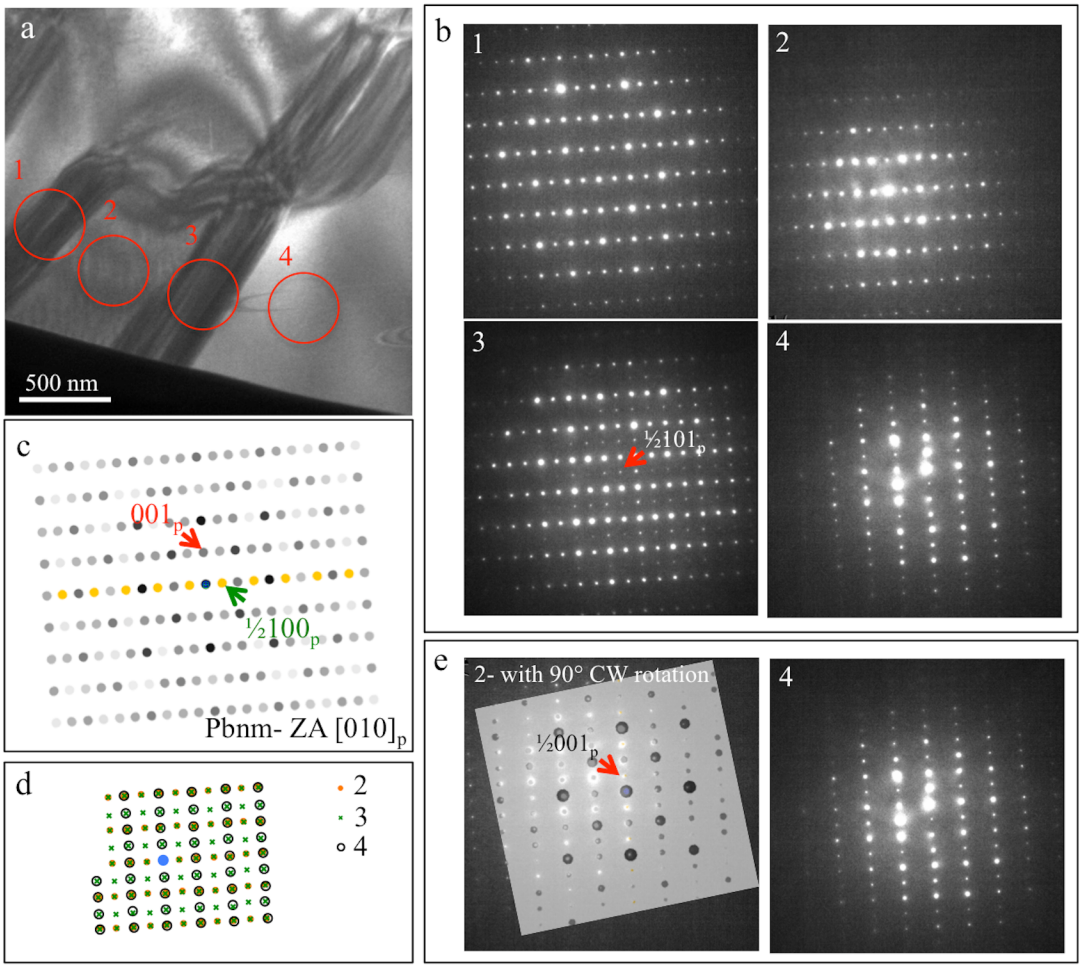

Figure 2- CLTO x = 0.1 specimen (prepared via FIB) (a) showing the BF micrograph with bands of defects, across which selected area diffraction patterns where acquired. Areas marked in (a) correspond to the numbered diffraction patterns in (b). The zone axis is along $[010]_p$ of the pseudo-cubic lattice (or 110 of the Pbnm orthorhombic unit cell). The simulation in (c) is the dynamical diffraction pattern assuming 200 nm thickness and the reported crystallographic parameters in Zhang et al.. The coloured spots show potential for double diffraction. (d) Schematic of diffraction peak positions in datasets 2, 3, and 4. (e) Compares diffraction (2) with 90 degrees CW rotation with pattern (4).

with the simulated kinematical pattern (using the structure reported in Zhang et al.[19]), with the reflection at $½100_p$ present. Pattern 2 shows a similar configuration, whereas in pattern 3 the coexistence of $½100_p$, $½101_p$, and $½001_p$ is observed. In pattern 4, if the same zone axis and in-plane orientation is assumed, $½001_p$ gains intensity whereas $½100_p$ vanishes. From this, we infer that the reflection observed at $½100_p$ cannot be due to double diffraction, as in that case it would be expected to exist across all patterns. Furthermore, close inspection of patterns 2 and 4 indicates that they differ through a 90° rotation, demonstrated in Figure 2(c).

From prior neutron diffraction analysis,[19] it is known that the Pbnm symmetry within the CLTO system corresponds to $a^-a^-c^+$ tilting. Woodward and Reaney[32] suggest this gives rise to the presence of ½(eeo) reflections (e: even; o: odd) on [100] or [010] zone axis patterns. Since this is a mix of in-phase and

anti-phase tilts, we can expect to observe ½{oee} reflections; however, these reflections can also indicate antiparallel cation displacement. Hence, the presence of $½001_p$ and $½101_p$ can correlate to mixed octahedral tilting. The presence of $½100_p$ in patterns 1 and 2 seems to be an outlier, which could be resolved by indexing these two patterns in the same zone axis but with a 90° in-plane rotation, Figure 2(c). This suggests that in the region shown, when passing across the band highlighted in #3, the crystal rotates 90°, i.e. the region in #3 is a $90°[010]_p$ tilt boundary, with the beam incident along the tilt axis. Note that the diffraction peaks in #3 can be accounted for by superimposing the two patterns in #2 and #4, except the $½101_p$ peaks (See schematic in panel (d)). It is possible that this boundary in #3 is inclined to the incident electron beam. In that case, it is expected to merely observe superposition of patterns from the adjoining grains in the region of the boundary. The presence of the $½101_p$ peaks seems to reject this scenario. The appearance of this reflection suggests a mechanism that accommodates changes in tilt directions of the octahedra. From a broader perspective, it can be seen that the tilting of the TiO_6 octahedra is clearly not the same across the bulk with regions separated by transition bands / defects. A similar observation of such lattice tilt rotation in x= 0.1 CLTO is presented in Figure S1 in the supplementary section.

In order to examine different zone axes, crushed powder samples were prepared and Figure 3 shows high resolution images from x = 0.2 with the electron beam incident along the $[010]_p$ direction (Similar to Figure 2). Pairs of HAADF / BF STEM micrographs are shown in panels (a) and (b), with a low magnification image of the particle included as an insert in (a) (a selected area diffraction pattern collected at low magnification is presented in the supplementary section, Figure S2). The variations in intensity in HAADF images correspond to varying distributions of La versus Ca in A-site positions, with La-rich columns appearing brighter in intensity. Atomically resolved core-loss electron energy-loss spectra were gathered along this zone axis to directly map the distribution of Ca versus La-rich columns. The area marked in the HAADF micrograph in Figure 3(c), acquired along the same zone axis as above-with only a scan rotation, is representative of such EELS measurement. The sum of the electron energy-loss spectrum across the entire spectrum image area, Figure 3(d), shows the characteristic Ca-$L_{2,3}$, Ti-$L_{2,3}$, O-K, and La-$M_{4,5}$ excitation edges. In Figure 3(e), along with the HAADF signal gathered during the spectrum image acquisition, elemental intensity maps, after background subtraction, are shown. The intensity maps of Ca and La in panel (e) show their respective distributions on the A-site, with high occupancy of one species resulting in lower intensity of the other. Domain boundaries, previously observed in Figure 2, were not encountered during high magnification STEM / EELS examination along this zone axis. Given the large size and low number density of such domains, this is not surprising.

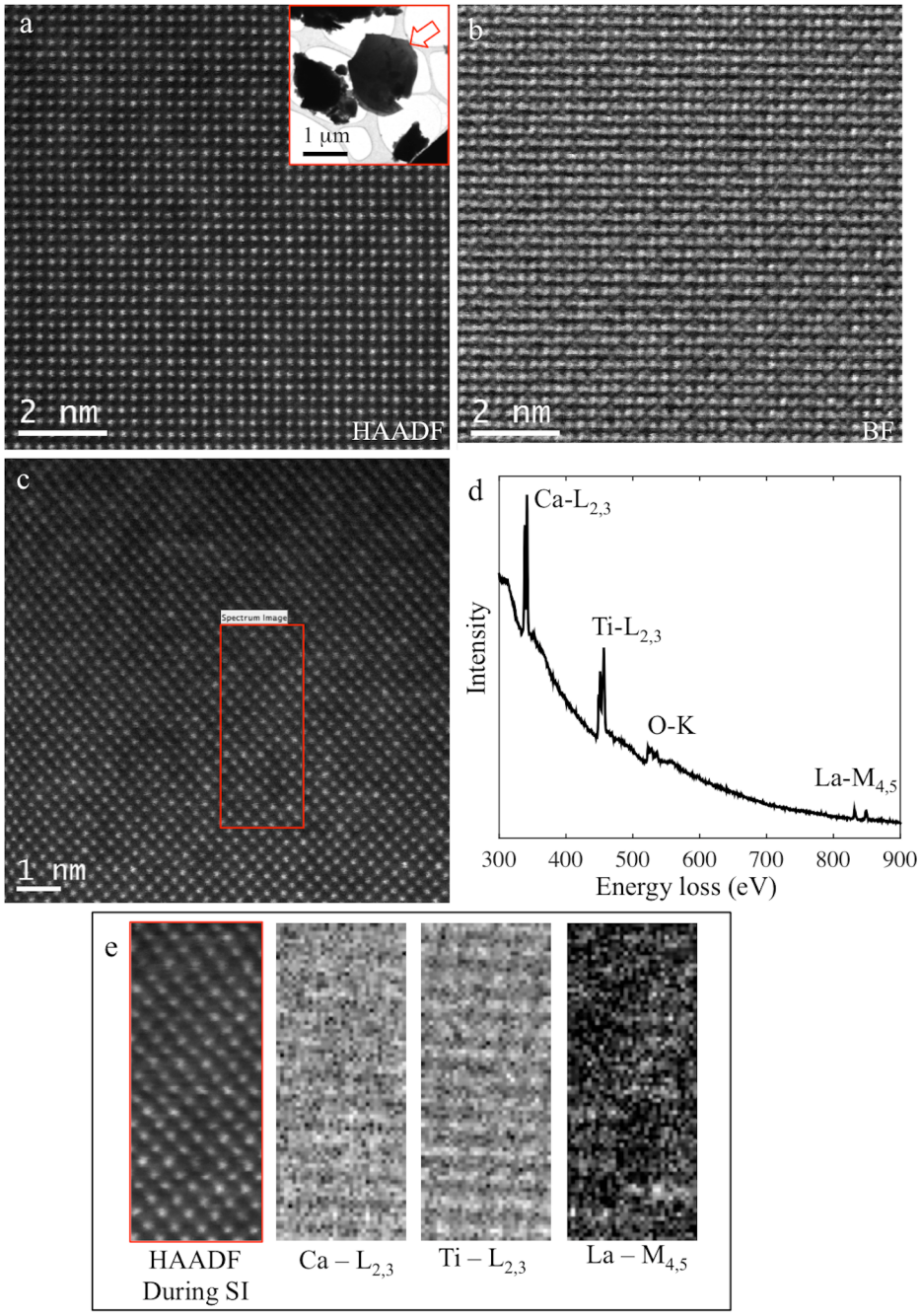

Figure 3 - CLTO x = 0.2 specimen (crushed grain sample) viewed along $[010]_p$ ZA – the low magnification image of the particle used for these datasets is included as inset in (a) HAADF image. (b) BF signal acquired simultaneously with (a). (c) HAADF image close to area in (a) with applied scan rotation. Region in red frame was selected for EELS spectrum imaging. (d) EELS sum spectrum of the region in (c). (e) HAADF during SI acquisition image along with elemental intensity maps.

Other boundaries indicating octahedral tilting were nevertheless observed at other zone axes, as described later in this section.

The x = 0.2 CLTO perovskite along the $[001]_p$ zone axis was examined across different particles (Figures 4 and 5). In Figure 4, the HAADF signal again shows variations in intensity, due to variations in La / Ca and A-site vacancy distribution. The concurrently acquired BF signal, panel (b), shows a

single domain, indicating no alteration in octahedral tilting within this region. Multislice simulations of expected HAADF and BF images, shown as lower insets in both panels, show a close match at a crystal thickness of 20 unit cells. The contrast observed in BF could be only reproduced with assuming a small tilt in the electron probe with respect to the sample, possibly due to local sample bending (here the case for 4 mrad tilt is presented). We recognise that the fit between the simulated and experimental BF is not ideal. This is due to the small size of the BF detector (3.4 mrad half-angle) compared to the probe convergence semi-angle (32 mrad), potentially resulting in misalignment. Nevertheless, we can show that the elongated features in the BF image can result from beam tilt. A matrix of BF and HAADF image simulations with varying sample thickness and probe tilts is shown in Figure S4 in the supplementary section. The HAADF signal was not as affected by the probe tilt compared to the BF signal. In fact several publications, e.g. Yamazaki et al.,[33] have previously shown that crystal tilt does not significantly move peak intensities in HAADF, and just alters their relative intensities.

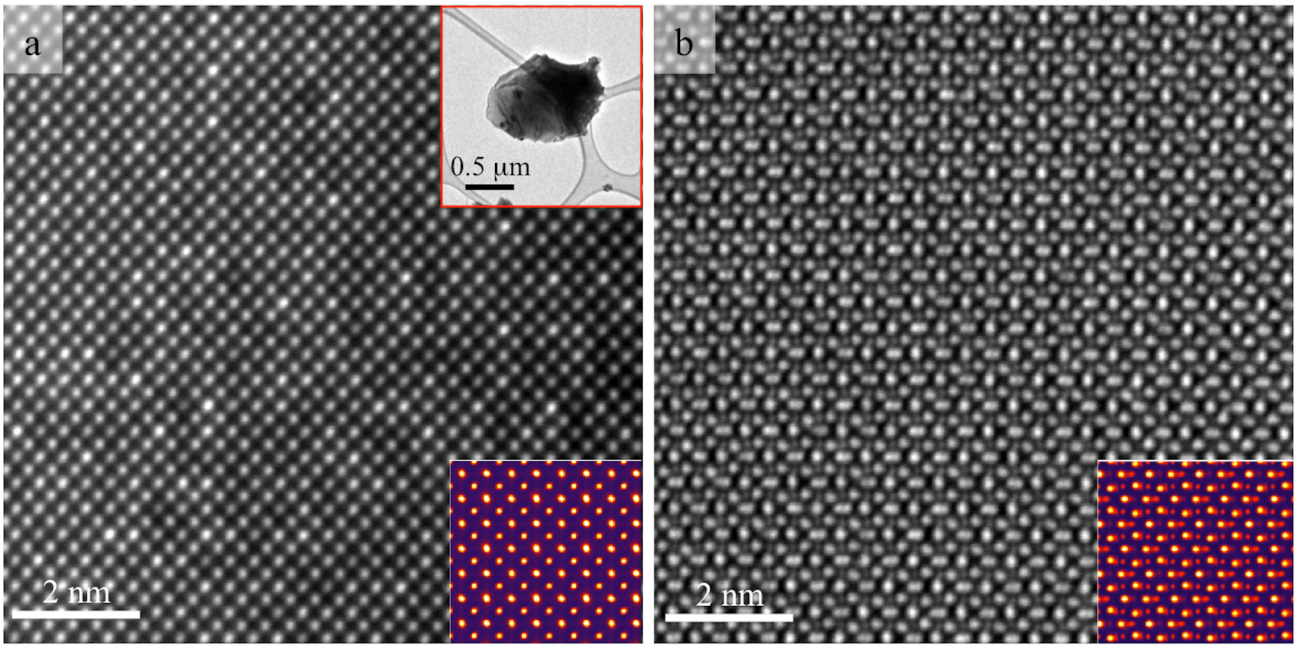

Figure 4 - CLTO x = 0.2 specimen (crushed grain sample) viewed along $[001]_p$ zone axis - the low magnification image of the particle used is shown as the upper inset in (a). (a) HAADF and (b) BF signal pairs acquired simultaneously. Lower insets are multislice simulations of HAADF and BF signals with 4 mrad probe tilt at 20 unit cells crystal thickness. An array of simulations for BF signal, with changes in crystal thickness and probe tilt, is presented in the Supplementary section.

In Figure 5, projecting along a similar zone axis but from a different particle, a generally similar HAADF contrast is observed, panel (a), however, the simultaneously acquired BF signal, panel (b), shows domains. These domains, as they only appear in the BF image, can be related to changes in the tilt orientation of TiO_6 octahedra. Using the routine described in the 'Experimental' section, mean 'unit cells' were constructed by averaging along the vertical axes of the HAADF and BF images, shown in panels (c) and (d). Since the variance in peak intensity for the B-sites (Ti) is much lower compared to

the shared A-sites (Ca / La), these two positions could be readily identified after applying the peak-finding routine. Using a matrix of fitted peak positions from the HAADF signal, the deviation from the mean position can be mapped across the image, panel (e). The A-sites are coloured according to the provided legend on the right-hand side, depending on the magnitude and the direction of displacement, relative to the neighbouring B-sites. The B-site positions (shown in smaller grey circles) were not included in the displacement map. The nominal displacement of the A-sites along $[100]_p$ and $[001]_p$ directions are also shown. The boundary evident in the BF signal coincides with change in A-site displacement, as measured from the HAADF image. On the right section of the displacement map in panel (e) the displacement matches closely the nominal configuration along $[001]_p$. On the opposite side of the boundary, however, this configuration is completely changed, appearing closer to $[100]_p$ configuration, indicating a $90°[010]_p$ tilt boundary.

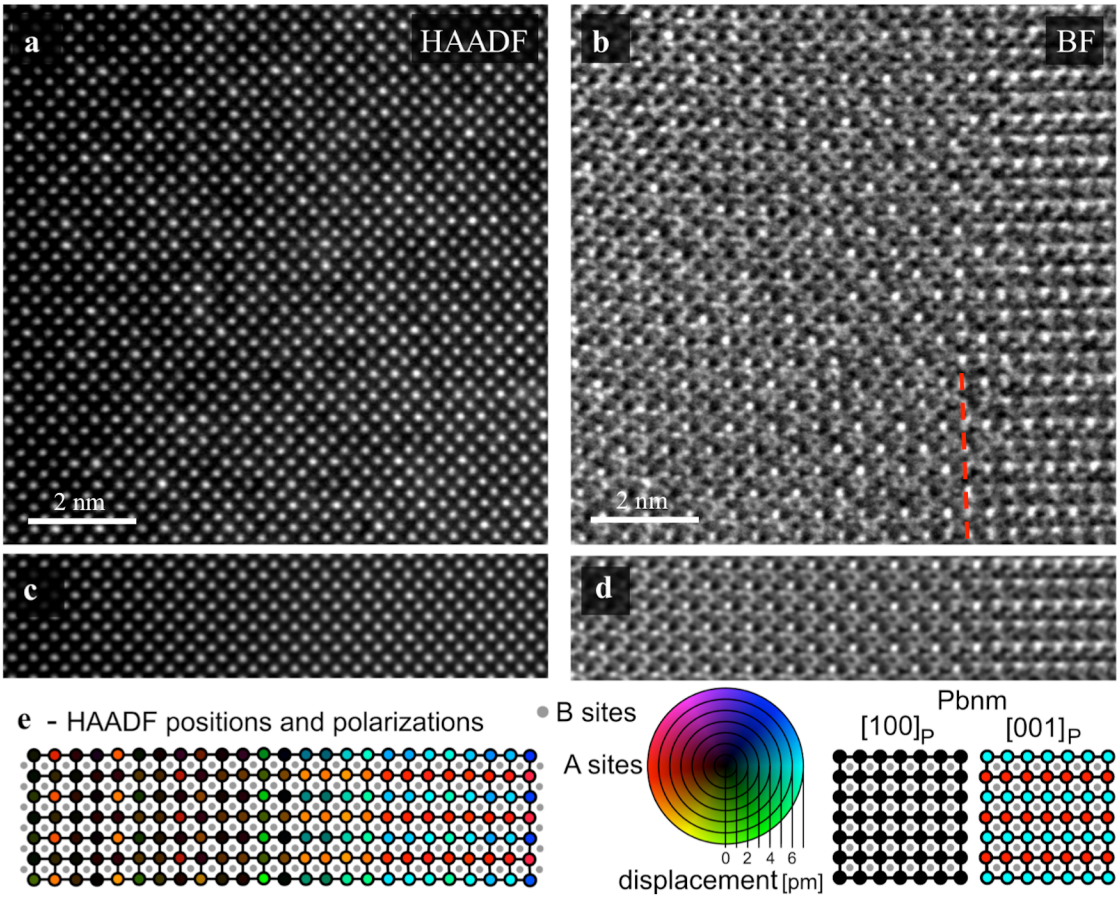

Figure 5 - CLTO x = 0.2 specimen (crushed grain sample) along $[001]_p$ zone axis: (a) HAADF, (b) BF signals acquired simultaneously. (c) and (d) 'unit cells' averaged along the vertical axes of images (a) and (b), respectively. (e) positions and displacements in A and B atomic sites, determined using the HAADF signal. Legend is provided on the right (B sites appear as grey; A sites are coloured according to magnitude and direction of displacement), with ideal atomic positions for $[001]_p$ and $[100]_p$ projections. The dashed line in (b) roughly marks the location of the boundary.

To highlight the changes in octahedral tilts, STEM measurements along the $[110]_p$ zone axis were undertaken, shown in Figure 6. Along this axis, similar boundaries – with pronounced presence in BF,

panel (b) in Figure 6, as opposed to a less obvious presence in HAADF signal, panel (a) – were observed. Windowed Fast Fourier transformations (FFT) of the marked areas in (b), are shown in panels (c) and (d). The differences between the two FFTs are the presence of $½111_p$ spot in (c) (marked with arrow) and its absence in (d). This can be explained by indexing the FFT in (c) as the $[010]_{Pbnm}$ zone axis and the FFT in (d) as $[100]_{Pbnm}$ (Note that these would correspond to $[110]_p$ / $[-110]_p$ directions in

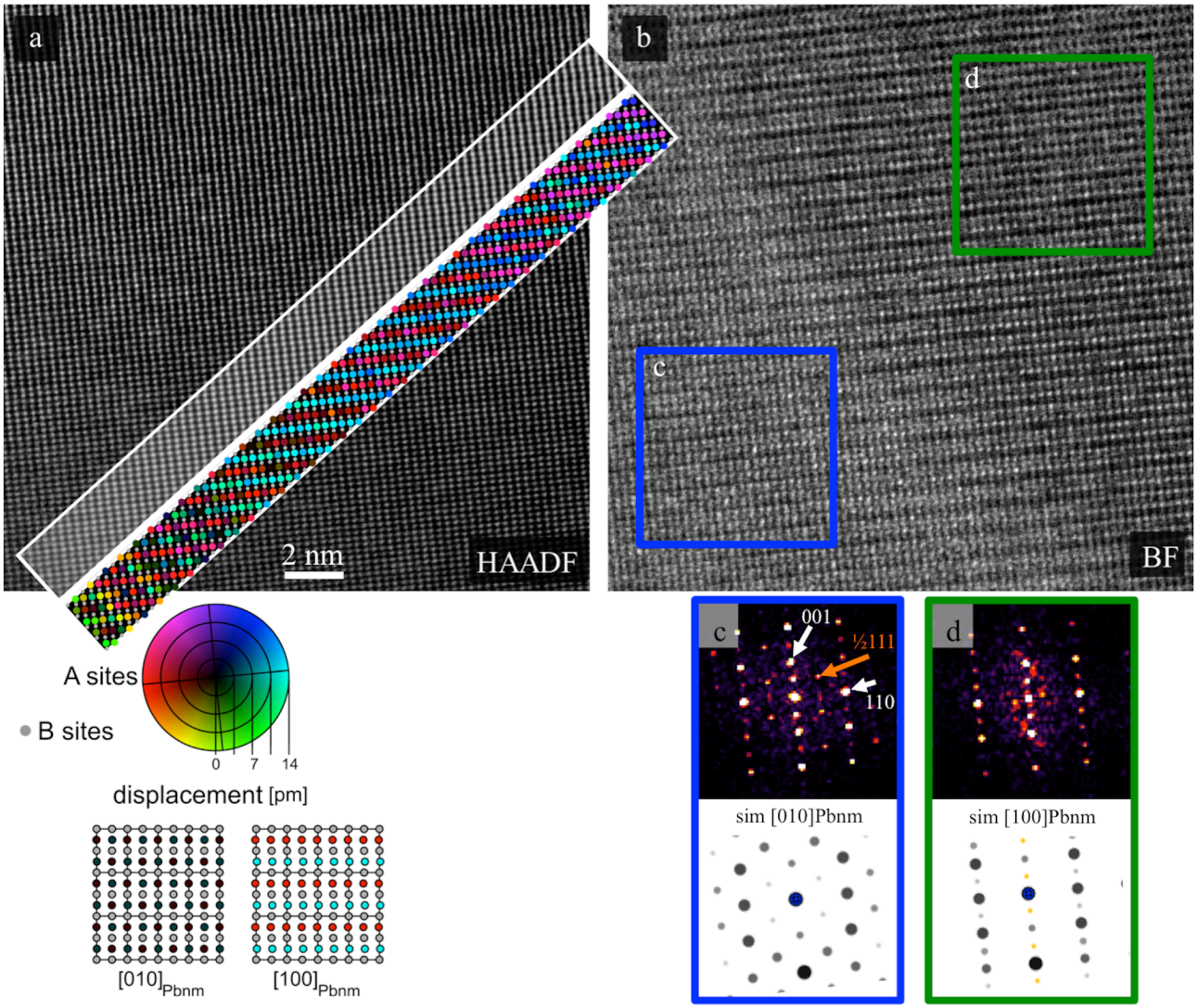

Figure 6 - CLTO x = 0.2 along $[110]_p$ zone axis: (a) HAADF and (b) BF images acquired simultaneously. The window over panel (a) contains both the averaged unit cell (measured along the shown direction from the HAADF image) and the A-site displacement map (B-sites appear as grey). Below panel (a) a legend for the map is provided, along with nominal displacement states along $[010]_{Pbnm}$ and $[100]_{Pbnm}$ directions. Frames in (b) mark the locations corresponding to fast Fourier transforms in panels (c) and (d), respectively. In each case, a diffraction simulation is presented. (Low magnification image of the particle used and corresponding SAD is shown in Figure S5.)

pseudo-cubic cell). Simulations of diffraction patterns along those two zone axes are shown in panels (c) and (d) for clarity. In the case of $[010]_{Pbnm}$, the mixed tilt system ($a^-a^-c^+$) gives rise to the appearance of the $½111_p$ reflection. Crystal models along the two directions are presented in both cases, signifying that the atomic positions, aside from the O^{2-} ions, are very similar. This provides an explanation for the

observed HAADF signal, showing only one single domain in Figure 6(a), since this signal is not affected by the O^{2-} ions. Superimposed on the HAADF micrograph (panel (a)) is the averaged unit cell, along with the A-site displacement map, with the legend provided. The upper right corner of the image matches closely in A-site displacement with the nominal Pbnm configuration along the $[100]_{Pbnm}$ zone axis (note the ideal crystal structure shown below). However, in the lower left section we observe a more random displacement, in-line with the $[010]_{Pbnm}$ zone axis. This agrees with the observation from the FFT of the BF signal, as shown in panels (c) and (d). Given the above, the boundary observed in BF signal, panel (b), comprises a tilt boundary with 90° rotation around $[001]_p$ axis, i.e. $90°[001]_p$, imaged with the electron beam incident perpendicular to the tilt axis.

3-3- Electron microscopy characterisation- CLTO with high La content (x = 0.9)

For the La-rich CLTO sample (x = 0.9) X-ray diffraction identified the structure as orthorhombic, adopting Cmmm symmetry. Figure 7(a) presents a low magnification STEM-DF image from such a composition, prepared via the FIB lift-out procedure. The orientation of the grain on the right hand side of the image was adjusted in parallel beam illumination (TEM) mode to be along $[110]_p$ zone axis. The TEM-BF image taken from the same zone axis is presented in the supplementary section (Figure S6). The corresponding selected area diffraction pattern, along with a simulation, is shown in panel (b). It can be observed here that ½001, ½1-10, and ½1-11 peaks are also present in this pattern. Each grain, as evident in panel (a), consists of twin-like domains. Since the small size of these domains made it difficult to capture isolated electron diffraction patterns in TEM mode, we acquired small convergence angle electron diffraction (CBED) patterns in STEM mode instead, which has a finer spatial resolution. The spots marked in the STEM-DF image, with numbers 1 through 6, designate the locations of the probe corresponding to the CBED patterns shown in panel (c). Here, it can be observed that the appearance of the fractional diffraction peaks does not occur evenly across the domain structure within this grain. For instance, comparing #1, #2, and #3, ½111 peaks seem to be present in #2, but absent in cases of #1 and #3 (note arrows in #2). More drastically this can be recognized for the case of patterns #4, #5, and #6, where the ½001 spot is strongly present in #5 and absent in the other two (arrowed). A lower intensity can also be discerned where ½1-10 reflections are expected to be present. This clearly demonstrates that the TEM selected-area diffraction pattern (Figure 7(b)) is an averaged diffraction signal with contributions from all of the sub-domains, averaged across the entire grain. STEM / CBED measurements show that each domain is associated with a slightly modified symmetry: ½001 pointing towards doubling of the c axis and ½111 indicating deviation from $a^-b^0c^0$ tilt system for the Cmmm symmetry (Cm2m symmetry with $a^-b^0c^+$ tilt could explain this superstructure reflection).[34] What is

important to note here is the smaller scale, and consequently higher number density, of such domains compared to those observed earlier in low La-content CLTO samples (Figure 2).

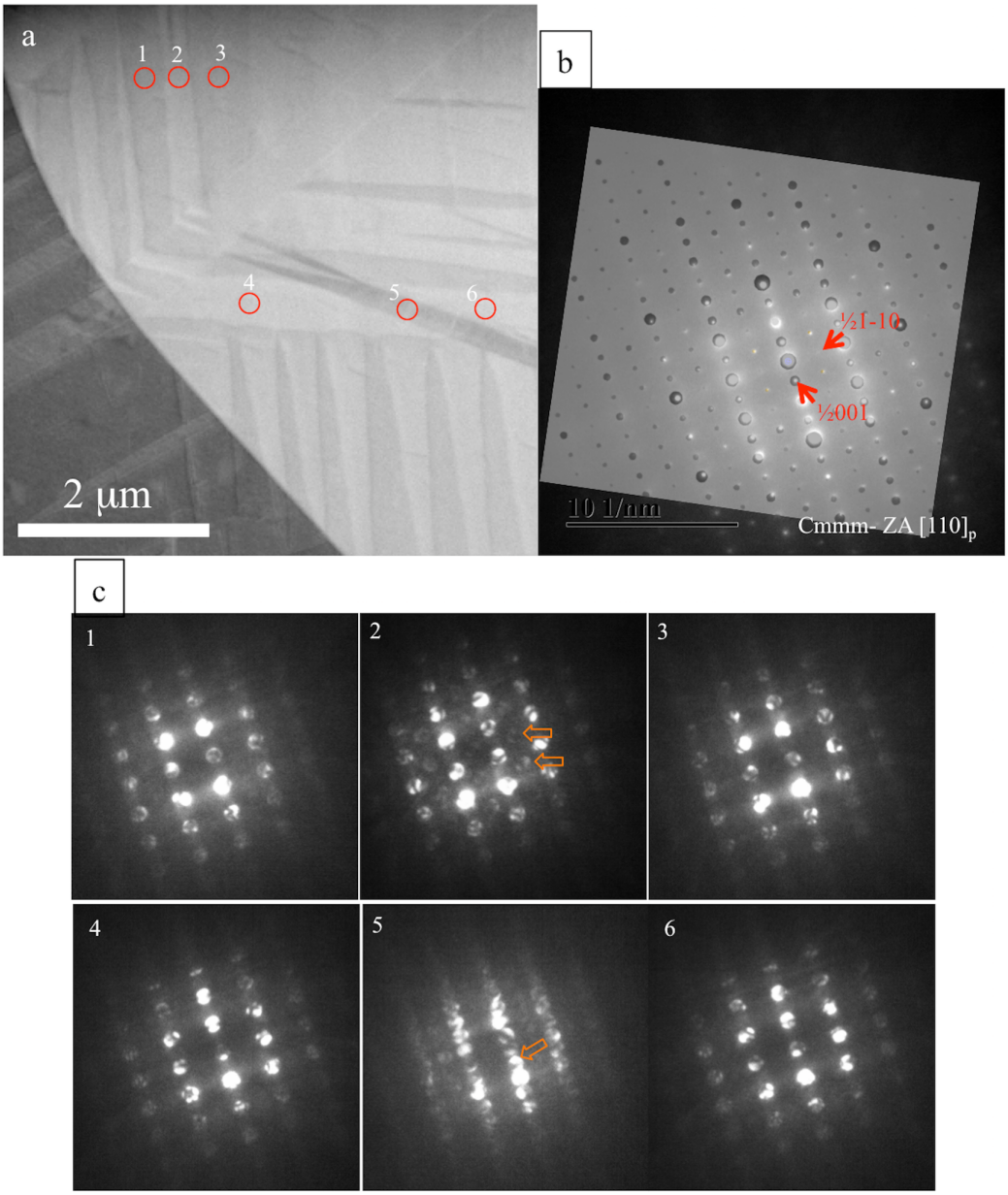

Figure 7 - CLTO x = 0.9 specimen (prepared by FIB) (a) low magnification STEM-DF image. The parallel beam diffraction pattern in (b) is acquired in TEM mode (at the same sample tilting conditions) from the right hand side "grain" in (a). The red circles in (a) mark the spots used for CBED observations in shown in (c). TEM bright-field image of the same region in (a) is presented in Figure S6 in the supplementary section.

For a more detailed analysis on the nature of the observed domains above, crushed powder samples were studied using aberration-corrected STEM / EELS. One CLTO x = 0.9 particle oriented along the $[100]_p$ zone axis, imaged using the HAADF detector, is shown in Figure 8. In the upper region of the HAADF image in panel (a), lines of higher intensity, distributed with no long-range ordering, are observed. Core-loss EELS spectrum imaging from a selected region, shown on the right hand side of

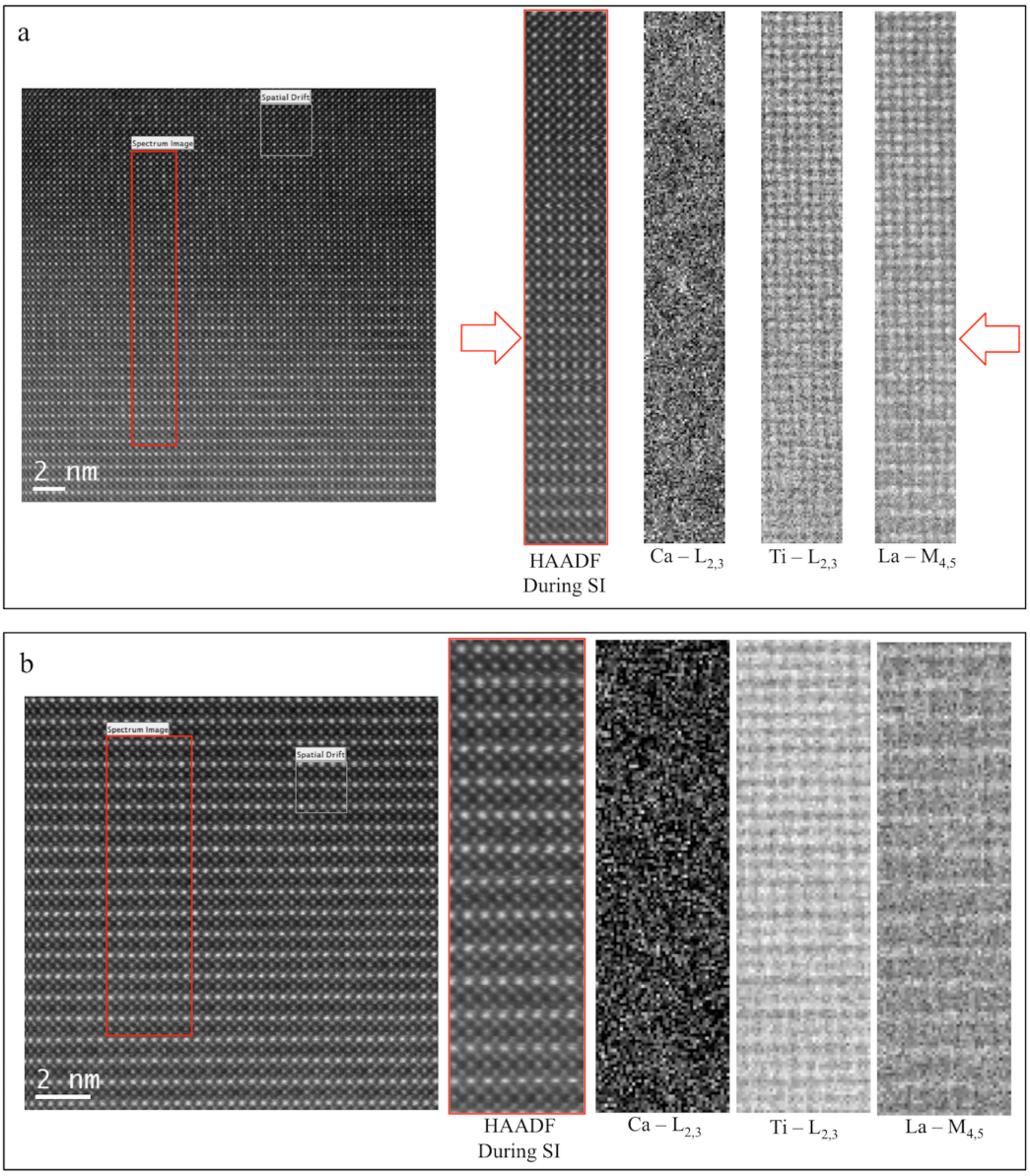

Figure 8 - CLTO x = 0.9 specimen (same particle as in Figure 9) along $[100]_p$ zone axis (a) HAADF image of an area with transition from single perovskite structure (top half) to double-layered perovskite (bottom half- the arrows roughly points to the transition region); on the right, the HAADF signal gathered during SI acquisition and the raw elemental maps from corresponding characteristic edges. (b) HAADF image from an area with long-range ordering double-perovskite structure (left), with HAADF signal taken alongside SI and maps (right).

panel (a), indicates that the line formations with higher HAADF intensity are comprised of La-rich columns. The Ca signal is noisier than the La signal due to proximity to the C-K edge (and resulting difficulties in obtaining a good background subtraction), but does not indicate any ordering. This regime was not persistent across the entire particle. In the lower half section of the same image, the '*random*' perovskite structure – this is not entirely random, given the presence of line clusters of La described above- transforms into a double perovskite structure, with doubling of the c axis. The La-$M_{4,5}$ map highlights this transition, with the upper half corresponding to the primitive pseudo-cubic perovskite unit cell and the lower half demonstrating condensation of La ions on alternating (001) planes, doubling

the c axis in the cubic unit cell. The arrows beside the HAADF, acquired during spectrum imaging, and the La map point roughly to where the transition takes place. Figure 8(b) shows an area away from the transition zone and entirely showing the double-perovskite ordering regime. Here the La-$M_{4,5}$ map, in confirmation of the observed HAADF intensity variations, shows a doubling of the primitive c-axis and preferential ordering of La ions and vacancies. It should be noted that the 001 planes with less intensity in the HAADF signal are not fully devoid of La, as is evidenced by the occasional high-intensity column on the vacancy-rich planes (also observed in the La map).

Within the particle above with long-range La^{3+} / V_{Ca}^{2-} ordering, twins were also encountered. Figure 9(a) and 9(b) are HAADF and BF pair images showing a twin boundary, with a low magnification view of the corresponding region presented as inset in panel (a) (arrowed). The twin boundary corresponds to ~ 90° rotation in the lattice (~ 0.6° deviation), hence the twin can be identified as a $90°[100]_p$ tilt boundary. The core-loss EELS spectrum image, shown in the supplementary section (Figure S7), confirms a direct correlation between the columns with high intensity to higher concentrations of La. Alongside this rotation in the double-perovskite structure, evident in the HAADF image, the BF signal indicates a change moving across the twin boundary. In the same particle, another boundary configuration of two meeting ordered double perovskite domains was observed. In this case, as shown in panels (c) and (d) in Figure 9 (pair HAADF / BF images), the La-rich planes in the first domain, upon passing through a transitional boundary, turn into vacancy-rich planes in the second domain and vice versa. This boundary can be identified as an $180°[100]_p$ tilt boundary.

In order to better resolve the changes in the octahedral tilts and investigate the ordering behaviour of the vacancies at a different projection, STEM analysis was performed along the $[110]_p$ zone axis of the Cmmm structure, shown in Figure 10. In panel (a) the HAADF signal at relatively low magnification (20 nm field of view) shows an area, which includes both the 'random' single unit cell perovskite structure and a highly ordered double perovskite region. Two regions, falling into the random and the ordered domains, are marked in (a), with corresponding FFTs shown in panel (b). It can be seen that $½001_p$ peaks are present in the ordered region (#2) that are absent in the single perovskite domain (#1).

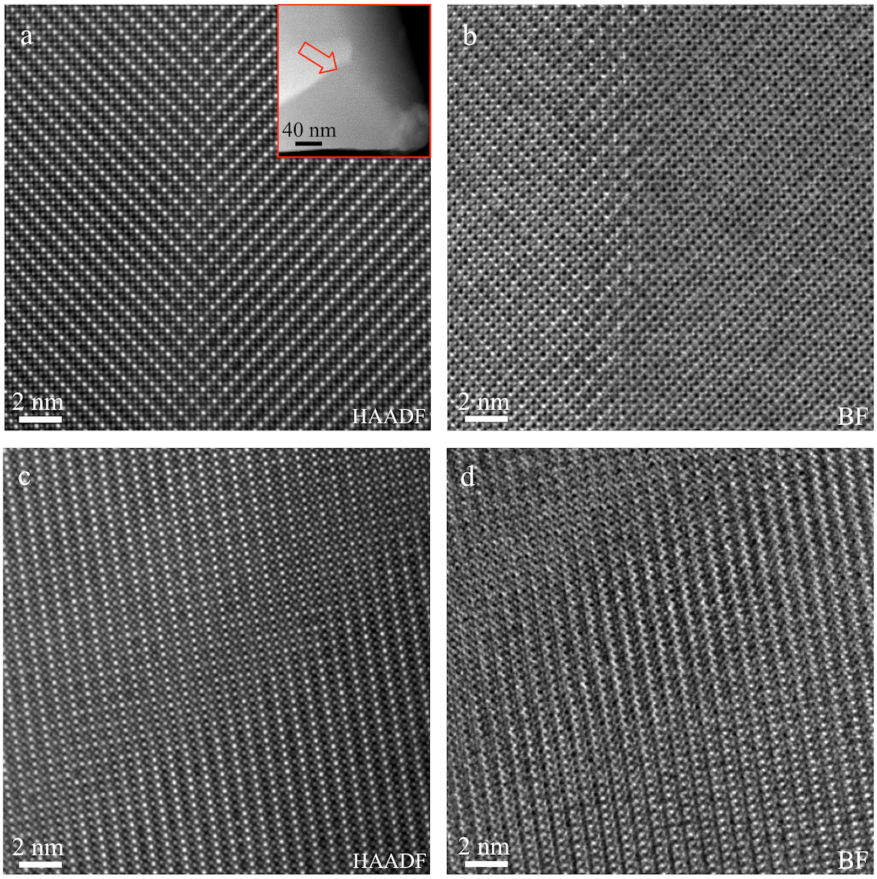

Figure 9 - CLTO x = 0.9 specimen (same particle and zone axis as the previous figure) (a) HAADF and (b) BF pair images showing a twin-like boundary. The inset in panel a shows the region with the twin at low magnification. (c) and (d) HAADF / BF image pair within the same particle showing another type of boundary between two double perovskite domains.

This observation is in-line with Figure 7, comparing point diffraction patterns #4, #5, and #6, with location corresponding to #5 marker having a double perovskite ordered structure. Similar bands of double perovskite domains were observed in the same particle as shown in Figure 10. Panels (c) and (d) present LAADF (low-angle annular dark-field) / ABF (annular bright-field) images highlighting the transition from a single to a double perovskite structure. High magnification LAADF / ABF micrographs from the ordered domain, panels (e) and (f), point to variations in La^{3+} occupancy on the $(001)_p$ planes. Crystal models along the same zone axis are superimposed in panels (c) and (d),

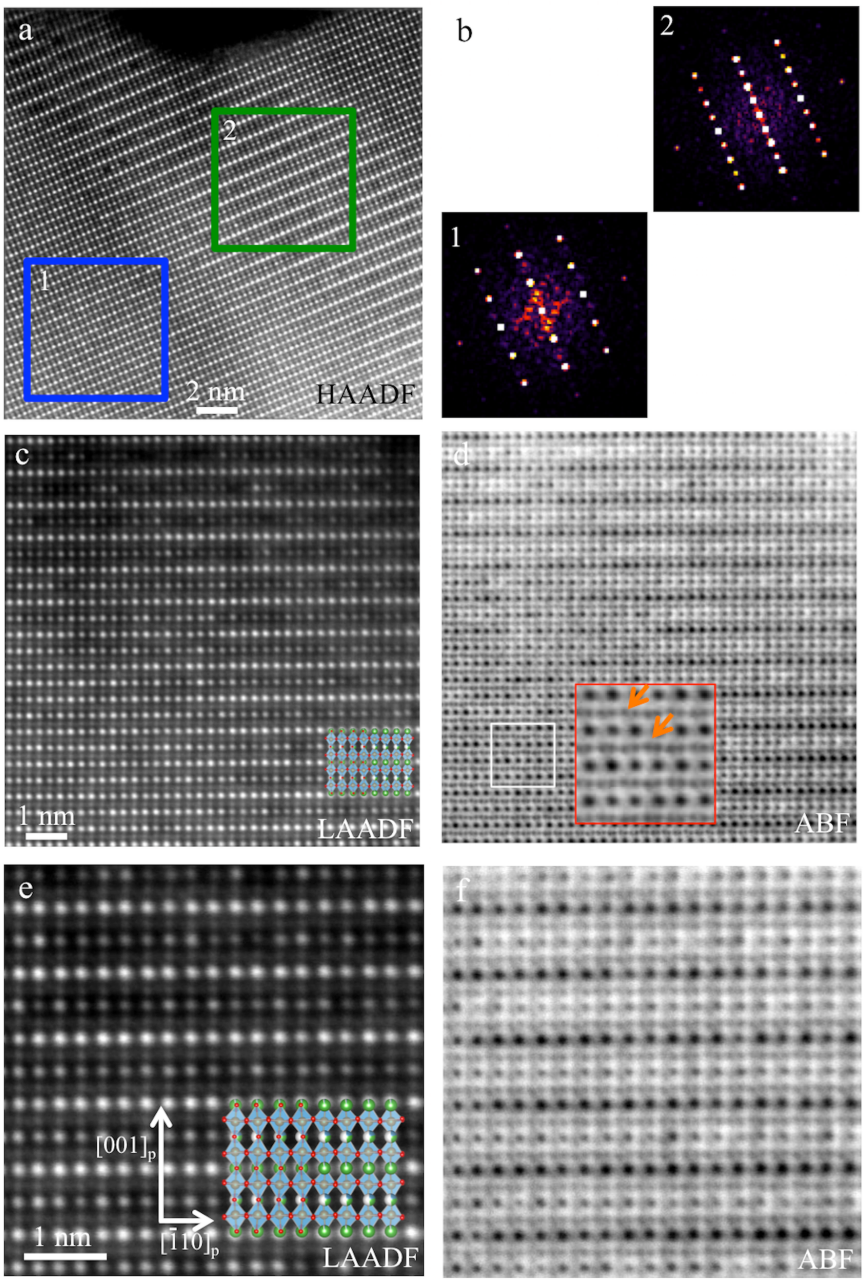

Figure 10 - CLTO x = 0.9, along $[110]_p$ zone axis: (a) HAADF image with 20 nm FOV, (b) FFT from the marked regions in (a). (c) and (d) LAADF and ABF pairs at 10 nm FOV at the transition regions. (e) and (f) LAADF and ABF pairs at 5 nm FOV from the double perovskite domain. Crystal models are superimposed in panels (c) and (e). Inset in (d) is detail of the marked area with white box on the left hand side. [Colour scheme in the crystal models: Ti orange, O red, Ca blue, and La green]

highlighting the feature of this zone axis that neighbouring atomic planes, perpendicular to $[001]_p$, alternate between (Ca,La) / O planes and Ti / O planes. It can be observed in panel (f) that O sites within the double perovskite domain do not show deviation from the crystal model. In contrast, close inspection of the single perovskite region, highlighted area in panel (d), clearly shows distortions in the O lattice (examples marked by arrows). In order to accurately map the displacement of the cations along this zone axis, an HAADF image - after applying non-linear scanning drift correction - was used, as

shown in Figure 11(a). In panel (b), an averaged unit cell, based on the HAADF image, along with a displacement map of the cationic sites are presented. Comparing to the crystal model along the same zone axis, it appears that the Ti^{4+} cations are displaced towards the left hand side of the octahedral spaces. This observation is discussed in the following sections.

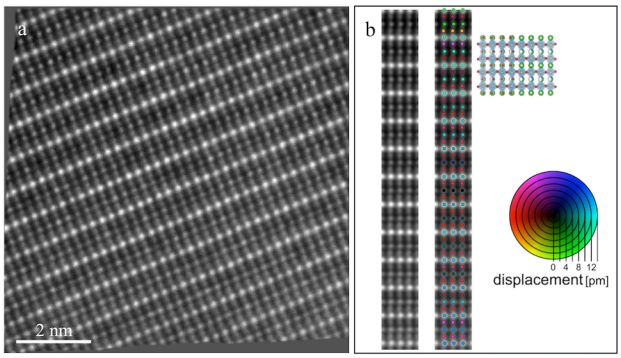

Figure 11 - CLTO x = 0.9, along $[110]_p$ zone axis: (a) HAADF image after non-linear scan drift correction, (b) averaged unit cell (left) and the displacement map (right) of the A and B-site cations. Legend for the magnitude and direction of the displacement is shown on the lower right. Crystal model along the same zone axis is presented for comparison.

4- Discussion

Comparing the two extremes in La composition within $Ca_{1-x}La_{2x/3}TiO_3$ perovskites, there is a strong tendency for the La-rich compositions to exhibit long-range vacancy ordering, whilst on the La-lean side, large domains were identified with extended defect structures, some of which are tilt boundaries. Observation of boundaries that were more prominently visible in the BF signal, and less so in HAADF, was recurrent. Analysis of the A-site displacement, mapped using the HAADF signal, was essential in identifying the nature of these boundaries. Even though the presence of these boundaries was readily recognized in BF image, due to sensitivity to both thickness and probe tilt, this signal was not suitable for quantifying atomic site positions. These boundaries proved to be tilt boundaries in all cases observed. In the Pbnm space group we have identified the following tilt boundaries: $90°[010]_p$ (twice), and $90°[001]_p$. In the Pbnm case, identification of such boundaries was not trivial and required access to both HAADF and BF (or ABF) signals. Whereas for Cmmm symmetry, discussed below, the tilt boundary was readily evident in the HAADF signal, as it is highlighted by change in the La^{3+} / V_{Ca}^{2-} ordering direction.

In the La-rich perovskite (x = 0.9), $Ca_{0.1}La_{0.6}TiO_3$, long range ordering in vacancies versus La^{3+} cations, with doubling of the $[001]_p$ axis of the pseudo-cubic unit cell was observed, in accordance with previous diffraction studies.[19] Our observations clearly demonstrate though that this doubling of the c_p axis

cannot describe the entire microstructure. These double perovskite regions either emerge from regions with random vacancy distribution (as shown earlier, both along $[100]_p$ and $[110]_p$), or are separated from other double perovskite regions by tilt boundaries. In the Cmmm case, two of the following boundaries were observed: 90°$[001]_p$ and 180°$[001]_p$. The boundaries within double perovskite domains were most prevalent in a FIB-prepared sample directly from the surface of the pellet. This could be due to higher vacancy concentrations closer to the surface, resulting in a higher number density of double-perovskite domains. Domains corresponding to octahedral tilt geometries different from the $a^-b^0c^0$ system, anticipated for the Cmmm symmetry based on the structure proposed by Zhang et al,[19] were also observed (i.e. ½111 reflection observed in panel (c) of Figure 7). It is known that thermal history plays an important role in the appearance or suppression of long-range vacancy / cation ordering in A-site deficient perovskites, with fast cooling rates arresting the necessary diffusional processes conducive to such ordering.[35,36] Given that the specimens examined here share the same thermal history, it strongly indicates that the observed disparity in ordering behaviour of V_{Ca}^{2-} / La^{3+} across the two ends of La compositions is a direct consequence of changes in chemistry.

A-site cation ordering in $AA'BO_3$ perovskites, as observed for x = 0.9 CLTO, is far less common than B-site cation ordering in $ABB'O_3$ perovskites;[37] but if present, A-site ordering almost exclusively adopts a layered ordering configuration.[38] Some other cases of columnar A-site ordering,[39] or a complex interplay between micro-twinning and columnar ordering[40] have also been reported. The more prevalent layered ordering results in differences of environment for anions, i.e. one-sixth of the anions are surrounded by four A cations while another one-sixth are surrounded by four A' cations. This bonding discrepancy is relieved, in perovskites with a highly charged d^0 cation on the B-site like Ti^{4+}, most preferably by the displacement of B-site cation towards the A-site cation layer with higher concentration of vacancies (this is known as Second Order Jahn-Teller (SOJT) distortion).[38,41] In our observations along $[110]_p$ zone axis of the x=0.9 CLTO, mapping the cationic displacements as presented in Figure 11, a shift in Ti^{4+} position towards the low occupancy $(001)_p$ plane was not observed, indicating that the SOJT mechanism suggested above is not active in this perovskite. Instead, a lateral shift in Ti within the octahedral spaces is observed, Figure 11(b). *Ab initio* calculations are needed to investigate the energetic favourability of this distortion mechanism versus the SOJT distortion suggested in other perovskites.

Layered ordering at the La-rich end of the $Ca_{1-x}La_{2x/3}TiO_3$ series has been observed in similar systems, e.g. $Sr_{1-x}La_{2x/3}TiO_3$,[42] and also in $La_{2/3}TiO_{3-\lambda}$,[13] with small oxygen deficiency (λ close to 0.007), as previously mentioned in the Introduction. A-layered ordering is also suggested to be present in $La_{2/3-x}Li_{3x}TiO_3$ (LLTO) and $La_{1/3-x}Li_{3x}NbO_3$ (LLNO) perovskites, with La-rich and La-poor planes

alternating along $[001]_p$ direction similar to x=0.9 composition of CLTO.[43–45] A combination of *ab initio* and Monte Carlo simulations on $Sr_{1-x}La_{2x/3}TiO_3$ suggests long-range ordering of the A-site as the contribution of vacant sites increases (larger x values).[46] According to this study, at low vacancy concentrations (V_{Sr}^{2-}) the electrostatic affinity between La^{3+} and V_{Sr}^{2-} dominates and these form neutral arrangements, e.g. linear or bent trimers, to minimize energy. In the presence of high vacancy concentration, the strain energy, favouring columns of neighbouring vacancies, outweighs the electrostatic interactions and leads to long-range ordering. This is suggested to arise from interplay between electrostatic forces (i.e. between La^{3+} and V_{Ca}^{2-}) and strain energy, with the latter being dominant for the case of long-range ordering of vacancy-La pairs at large x values. Nominally, in the x = 0.2 perovskite (with Pbnm symmetry) we expect around 7% vacancies on A sites, whereas, in x = 0.9 this amounts to 30%. Similar arguments could potentially apply for the CLTO system. An alternative crystal structure proposed for $La_{2/3}TiO_3$ entails layered ordering with 2 layers of high La occupancy and 1 layer of vacancy-rich configuration with I4/mmm symmetry and a = b = 3.856 Å and c = 24.6 Å.[17] Given out HAADF and EELS observations we can safely rule out the occurrence of similar ordering in La-rich CLTO perovskite.

In x = 0.9 CLTO, diffraction evidence was observed pointing to modified tilting configuration, deviating from the $a^-b^0c^0$ regime expected from Cmmm symmetry (Table 1), i.e. ½111 peak presence in Figure 7. A similar observation was reported for low Li-content $La_{2/3-x}Li_{3x}TiO_3$,[47] with the presence of ½111 peak indicating rhombohedral symmetry, where prior diffraction data suggested Pm-3m and P4/mmm symmetries with no octahedral tilting and hence requiring absence of peak at ½111 position. Regions with modified Ti-O tilting were shown to be responsible for this peak's presence. The same appears to be the case for x = 0.9 CLTO, as shown in Figures 10(d) and 11(b), with evidence of distortions in O and Ti lattices giving rise to ½111 peak. This is another aspect of the microstructure that was not detectable via volume-averaged diffraction measurements.[19]

A recent study on the similar A-site deficient perovskite system $Ca_{0.1}Nd_{0.6}TiO_3$ observed an incommensurate superlattice structure.[48] Taking up a morphology described as 'nanochessboard', these domains were shown to correspond to strain arising from modulations in the octahedral titling, and not from chemical segregation, as suggested in earlier studies on similar systems.[49,50] In $Nd_{2/3-x}Li_{3x}TiO_3$ perovskites analogous features in the microstructure, i.e. one or two-dimensional stripe patterns and nanochessboard arrangements were correlated with parallel ordering and spinodal decomposition along different crystallographic directions.[51] Similar behaviour was not encountered in CLTO. Instead, the

common structural feature in both extreme cases of composition in CLTO appeared to be the development of tilt boundaries, as was documented throughout this study. The prevalence of twinning and twin-like boundaries in perovskites was recognized from the very early days of optical crystallography investigations of natural $CaTiO_3$ minerals.[52] In the first detailed electron microscopy characterisation of $CaTiO_3$, White et al. identified two types of tilt boundary systems (See supplementary section, Figure S8, for conversion from reported Pcmn indices[53] to pseudo-cubic):[54] 90° and 180° rotation about normal to $(100)_p$. The former case was one of the boundary types observed in the present study. Interestingly, the LLTO system also demonstrated a high number density of 90° rotation boundaries, varying in size depending on the composition.[55] Similarly, doubling of the unit cell along with appearance of twinning with 90° rotation of the lattice was reported in $LaAlO_3$-stabilised $La_{2/3}TiO_3$.[56] A follow-up study on this system linked a higher number density of twins to faster cooling rates,[57] postulating that occurrence of these defects points to a mechanism that accommodates the induced strains through the phase transformations. Although we have not investigated the effect of cooling rate on the twinning domains in CLTO, it is safe to infer a same trend. It is also possible that strain does not play a major role and we are observing the effect of change in space groups, modifying a crystallographic direction with high symmetry at elevated temperatures to a number of non-equivalent directions at a lower temperature, lower symmetry space group in neighbouring domains. More work is required to unequivocally resolve the above distinction.

Since the tilt boundaries observed in CLTO are accommodated by subtle changes in the octahedral spaces, they were not accompanied by complex boundary structures, such as those reported for $SrTiO_3$.[58,59] In those cases, as the boundary structure involved repeating patterns of Sr and Ti, they were readily recognizable in HAADF signal. A twin boundary in $CaTiO_3$ in one experimental study was associated with polarisation in Ti, with 3 to 6 pm deviation from the zero-polarity position,[60] pointing to very localized ferroelectric domain with a non-polar matrix. However, this was not observed in the boundaries examined here, namely, the polarisation in Ti was close to or smaller than our peak position precision of 3 pm.

5- Conclusions

Ordering in the A-site occupancy and the nature of the domain boundaries were characterized in the $Ca_{1-x}La_{2x/3}TiO_3$ perovskite structure using atomically resolved STEM / EELS analysis. In the low La-content regime, with Pbnm space group and examined along $[010]_p$, $[001]_p$, and $[110]_p$ zone axes, long-range ordering in La^{3+} or vacancies was not observed. Micrographs of HAADF signal pointed to

occasional linear configuration of La^{3+} ions. Tilt boundaries, with prominent contrast in BF images but almost invisible in HAADF signal, were commonly observed. In this composition range we identified the following tilt boundaries: $90°[010]_p$ (twice), and $90°[001]_p$. Successful characterisation of these boundaries was only possible through simultaneous access to both BF and HAADF signals, and applying a detailed peak-finding and displacement-mapping routine to the HAADF image.

In the La-rich end of the composition, with Cmmm space group and examined along the $[100]_p$ and $[110]_p$ zone axes, long-range ordering of vacancies and La^{3+} ions was observed. This was demonstrated with alternating La-rich and La-poor layers on $(001)_p$ planes, effectively creating a double perovskite lattice along the c axis. These highly-ordered domains were observed to be either isolated within a 'matrix' of random distribution of vacancies / La^{3+}, or found with a high number density, covering nearly an entire particle. In regions with a high population of double perovskite domains, these ordered regions were separated from each other by tilt boundaries, with 90° or 180° misorientation across the two neighbouring grains. Observation of $½111_p$ peak in the high La-content CLTO electron diffraction patterns was correlated to regions with distortions in O-Ti bonds.

Acknowledgements

Funding is acknowledged from the UK's Engineering and Physical Sciences Research Council (EPSRC) under grants EP/K029770/1 and EP/L005581/1. PDE acknowledges support from the U.S. Department of Energy, Office of Science, Fusion Energy Sciences. SML acknowledges funding from the EPSRC grant EP/G037140/1. SuperSTEM is the UK National Facility for Aberration-Corrected STEM, supported by EPSRC. Work at the Molecular Foundry was supported by the Office of Science, Office of Basic Energy Sciences, of the U.S. Department of Energy under Contract No. DE-AC02-05CH11231. Guidance in sample preparation from Dr. Amy Gandy is gratefully acknowledged.

Supporting Information Available: Second example of tilt boundary observed in x = 0.1 CLTO. Low magnification images of the particles used for Figures 3, 4, 6, and 7 along with corresponding SAD patterns. Array of multislice simulations for BF and HAADF signals, CLTO x = 0.2, with changes in thickness and probe tilt. EELS map of area shown in Figure 9(a). Comparing Pbnm and Pcmn unit cells.

References

(1) Vashook, V.; Vasylechko, L.; Knapp, M.; Ullmann, H.; Guth, U. Lanthanum Doped Calcium Titanates: Synthesis, Crystal Structure, Thermal Expansion and Transport Properties. *J. Alloys Compd.* **2003**, *354*, 13–23.

(2) Kim, I.-S.; Jung, W.-H.; Inaguma, Y.; Nakamura, T.; Itoh, M. Dielectric Properties of a-Site Deficient Perovskite-Type Lanthanum-Calcium-Titanium Oxide Solid Solution System [(1 − x)$La_{2/3}TiO_3$ − $xCaTiO_3$ ($0.1 \leq X \leq 0.96$)]. *Mater. Res. Bull.* **1995**, *30*, 307–316.

(3) Salje, E.; Zhang, H. Domain Boundary Engineering. *Phase Transit.* **2009**, *82*, 452–469.

(4) Howard, C. J.; Lumpkin, G. R.; Smith, R. I.; Zhang, Z. Crystal Structures and Phase Transition in the System $SrTiO_3$–$La_{2/3}TiO_3$. *J. Solid State Chem.* **2004**, *177*, 2726–2732.

(5) Smith, K. L.; Lumpkin, G. R.; Blackford, M. G.; Colella, M.; Zaluzec, N. J. In Situ Radiation Damage Studies of $La_xSr_{1-3x/2}TiO_3$ Perovskites. *J. Appl. Phys.* **2008**, *103*, 83531.

(6) Ringwood, A. E.; Kesson, S. E.; Ware, N. G.; Hibberson, W.; Major, A. Immobilisation of High Level Nuclear Reactor Wastes in SYNROC. *Nature* **1979**, *278*, 219–223.

(7) Ali, R.; Yashima, M. Space Group and Crystal Structure of the Perovskite $CaTiO_3$ from 296 to 1720 K. *J. Solid State Chem.* **2005**, *178*, 2867–2872.

(8) Megaw, H. D. *Crystal Structures : A Working Approach*; Studies in physics and chemistry ; no. 10; Saunders: Philadelphia ; London, 1973.

(9) Glazer, A. Simple Ways of Determining Perovskite Structures. *Acta Crystallogr. Sect. A* **1975**, *31*, 756–762.

(10) Kestigian, M.; Ward, R. The Lanthanum-Titanium-Oxygen System. *J Am Chem Soc* **1955**, *77*, 6199–6200.

(11) MacLean, D. A.; Ng, H.-N.; Greedan, J. E. Crystal Structures and Crystal Chemistry of the $RETiO_3$ Perovskites: RE = La, Nd, Sm, Gd, Y. *J. Solid State Chem.* **1979**, *30*, 35–44.

(12) Eitel, M.; Greedan, J. E. A High Resolution Neutron Diffraction Study of the Perovskite $LaTiO_3$. *J. Common Met.* **1986**, *116*, 95–104.

(13) Abe, M.; Uchino, K. X-Ray Study of the Deficient Perovskite. *Mater. Res. Bull.* **1974**, *9*, 147–155.

(14) Inaguma, Y.; Liquan, C.; Itoh, M.; Nakamura, T.; Uchida, T.; Ikuta, H.; Wakihara, M. High Ionic Conductivity in Lithium Lanthanum Titanate. *Solid State Commun.* **1993**, *86*, 689–693.

(15) MacChesney, J. B.; Sauer, H. A. The System La_2O_3— TiO_5; Phase Equilibria and Electrical Properties. *J. Am. Ceram. Soc.* **1962**, *45*, 416–422.

(16) Lee, H. J.; Park, H. M.; Cho, Y. K.; Nahm, S. Microstructure Characterization of the (1−x)$La_{2/3}TiO_3$· $xLaAlO_3$ System. *J. Am. Ceram. Soc.* **2003**, *86*, 1395–1400.

(17) Gönen, Z. S.; Paluchowski, D.; Zavalij, P.; Eichhorn, B. W.; Gopalakrishnan, J. Reversible Cation/Anion Extraction from $K_2La_2Ti_3O_{10}$: Formation of New Layered Titanates, $KLa_2Ti_3O_{9.5}$ and $La_2Ti_3O_9$. *Inorg. Chem.* **2006**, *45*, 8736–8742.

(18) Vashook, V.; Vasylechko, L.; Trofimenko, N.; Kuznecov, M.; Otchik, P.; Zosel, J.; Guth, U. A-Site Deficient Perovskite-Type Compounds in the Ternary $CaTiO_3$-$LaCrO_3$-$La_{2/3}TiO_3$ System. *J. Alloys Compd.* **2006**, *419*, 271–280.

(19) Zhang, Z.; Lumpkin, G. R.; Howard, C. J.; Knight, K. S.; Whittle, K. R.; Osaka, K. Structures and Phase Diagram for the System $CaTiO_3$–$La_{2/3}TiO_3$. *J. Solid State Chem.* **2007**, *180*, 1083–1092.

(20) Aleksandrov, K. S.; BartolomÉ, J. Structural Distortions in Families of Perovskite-like Crystals. *Phase Transit.* **2001**, *74*, 255–335.

(21) Giannuzzi, L. A.; Stevie, F. A. A Review of Focused Ion Beam Milling Techniques for TEM Specimen Preparation. *Micron* **1999**, *30*, 197–204.

(22) Pennycook, S. J.; Nellist, P. D. *Scanning Transmission Electron Microscopy: Imaging and Analysis*; Springer Science & Business Media, 2011.

(23) Kim, Y.; Pennycook, S. j.; Kalinin, S. v.; Borisevich, A. y.; Yu, P.; Ramesh, R.; Chu, Y. Direct Mapping of Octahedral Tilts in Perovskite Oxide Materials Using Bright Field Scanning Transmission Electron Microscopy. *Microsc. Microanal.* **2012**, *18* (Supplement S2), 420–421.
(24) Zhu, Y.; Withers, R. L.; Bourgeois, L.; Dwyer, C.; Etheridge, J. Direct Mapping of Li-Enabled Octahedral Tilt Ordering and Associated Strain in Nanostructured Perovskites. *Nat. Mater.* **2015**, *14*, 1142–1149.
(25) Aso, R.; Kan, D.; Shimakawa, Y.; Kurata, H. Octahedral Tilt Propagation Controlled by A-Site Cation Size at Perovskite Oxide Heterointerfaces. *Cryst. Growth Des.* **2014**, *14*, 2128–2132.
(26) James, E. M.; Browning, N. D. Practical Aspects of Atomic Resolution Imaging and Analysis in STEM. *Ultramicroscopy* **1999**, *78*, 125–139.
(27) Stadelmann, P. JEMS JAVA electron microscopy software http://www.jems-saas.ch/ (accessed Dec 17, 2015).
(28) Ophus, C.; Ciston, J.; Nelson, C. T. Correcting Nonlinear Drift Distortion of Scanning Probe and Scanning Transmission Electron Microscopies from Image Pairs with Orthogonal Scan Directions. *Ultramicroscopy* **2016**, *162*, 1–9.
(29) Kirkland, E. J. *Advanced Computing in Electron Microscopy*; Springer Science & Business Media, 2010.
(30) Hitchcock, P. B.; Lappert, M. F.; Maron, L.; Protchenko, A. V. Lanthanum Does Form Stable Molecular Compounds in the +2 Oxidation State. *Angew. Chem. Int. Ed.* **2008**, *47*, 1488–1491.
(31) Shannon, R. D. Revised Effective Ionic Radii and Systematic Studies of Interatomic Distances in Halides and Chalcogenides. *Acta Crystallogr. A* **1976**, *32*, 751–767.
(32) Woodward, D. I.; Reaney, I. M. Electron Diffraction of Tilted Perovskites. *Acta Crystallogr. B* **2005**, *61*, 387–399.
(33) Yamazaki, T.; Kawasaki, M.; Watanabe, K.; Hashimoto, I.; Shiojiri, M. Effect of Small Crystal Tilt on Atomic-Resolution High-Angle Annular Dark Field STEM Imaging. *Ultramicroscopy* **2002**, *92*, 181–189.
(34) Kishida, K.; Goto, K.; Inui, H. Electron Diffraction of ABX_3 Perovskites with Both Layered Ordering of A Cations and Tilting of BX_6 Octahedra. *Acta Crystallogr. B* **2009**, *65*, 405–415.
(35) Howard, C. J.; Zhang, Z.; Carpenter, M. A.; Knight, K. S. Suppression of Strain Coupling in Perovskite $La_{0.6}Sr_{0.1}TiO_3$ by Cation Disorder. *Phys. Rev. B* **2007**, *76*, 54108.
(36) Labeauu, M.; Grey, I. E.; Joubert, J. C.; Vincent, H.; Alario-Franco, M. A. Structural Studies on A-Cation-Deficient Perovskite-Related Phases. II. Microdomain Formation in $ThNb_4O_{12}$. *Acta Crystallogr. A* **1982**, *38*, 753–761.
(37) Davies, P. K. Cation Ordering in Complex Oxides. *Curr. Opin. Solid State Mater. Sci.* **1999**, *4*, 467–471.
(38) King, G.; M. Woodward, P. Cation Ordering in Perovskites. *J. Mater. Chem.* **2010**, *20*, 5785–5796.
(39) Aimi, A.; Mori, D.; Hiraki, K.; Takahashi, T.; Shan, Y. J.; Shirako, Y.; Zhou, J.; Inaguma, Y. High-Pressure Synthesis of A-Site Ordered Double Perovskite $CaMnTi_2O_6$ and Ferroelectricity Driven by Coupling of A-Site Ordering and the Second-Order Jahn–Teller Effect. *Chem. Mater.* **2014**, *26*, 2601–2608.
(40) Labeau, M.; Grey, I. E.; Joubert, J. C.; Chenevas, J.; Collomb, A.; Guitel, J. C. The Structure of the A-Cation-Deficient Perovskite UNb_4O_{12}. *Acta Crystallogr. B* **1985**, *41*, 33–41.
(41) Knapp, M. C.; Woodward, P. M. A-Site Cation Ordering in $AA'BB'O_6$ Perovskites. *J. Solid State Chem.* **2006**, *179*, 1076–1085.
(42) Howard, C. J.; Zhang, Z. Structures and Phase Transition in the Layered Perovskite $La_{0.6}Sr_{0.1}TiO_3$: A New Orthorhombic Structure Solved from High-Resolution Diffraction in Combination with Group Theoretical Analysis. *J. Phys. Condens. Matter* **2003**, *15*, 4543.
(43) Catti, M. Ion Mobility Pathways of the Li^+ Conductor $Li_{0.125}La_{0.625}TiO_3$ by Ab Initio Simulations. *J. Phys. Chem. C* **2008**, *112*, 11068–11074.

(44) Gao, X.; J. Fisher, C. A.; H. Ikuhara, Y.; Fujiwara, Y.; Kobayashi, S.; Moriwake, H.; Kuwabara, A.; Hoshikawa, K.; Kohama, K.; Iba, H.; Ikuhara, Y. Cation Ordering in A-Site-Deficient Li-Ion Conducting Perovskites $La_{(1-x)/3}$ Li_X NbO_3. *J. Mater. Chem. A* **2015**, *3*, 3351–3359.
(45) García-Martín, S.; Alario-Franco, M. A.; Ehrenberg, H.; Rodríguez-Carvajal, J.; Amador, U. Crystal Structure and Microstructure of Some $La_{2/3-X}$ Li_{3X} TiO_3 Oxides: An Example of the Complementary Use of Electron Diffraction and Microscopy and Synchrotron X-Ray Diffraction To Study Complex Materials. *J. Am. Chem. Soc.* **2004**, *126*, 3587–3596.
(46) Thomas, B. S.; Marks, N. A.; Harrowell, P. Inversion of Defect Interactions due to Ordering in $Sr_{1-3x/2}La_xTiO_3$ Perovskites: An Atomistic Simulation Study. *Phys. Rev. B* **2006**, *74*, 214109.
(47) García-González, E.; Urones-Garrote, E.; Várez, A.; Sanz, J. Unravelling the Complex Nanostructure of $La_{0.5-x}Li_{0.5-x}Sr_{2x}TiO_3$ Li Ionic Conductors. *Dalton Trans.* **2016**, *45*, 7148–7157.
(48) Azough, F.; Kepaptsoglou, D.; Ramasse, Q. M.; Schaffer, B.; Freer, R. On the Origin of Nanochessboard Superlattices in A-Site-Deficient Ca-Stabilized $Nd_{2/3}TiO_3$. *Chem. Mater.* **2015**, *27*, 497–507.
(49) Guiton, B. S.; Davies, P. K. Nano-Chessboard Superlattices Formed by Spontaneous Phase Separation in Oxides. *Nat. Mater.* **2007**, *6*, 586–591.
(50) Withers, R. L.; Bourgeois, L.; Snashall, A.; Liu, Y.; Norén, L.; Dwyer, C.; Etheridge, J. Chessboard/Diamond Nanostructures and the A-Site Deficient, $Li_{1/2-3x}Nd_{1/2+x}TiO_3$, Defect Perovskite Solid Solution. *Chem. Mater.* **2013**, *25*, 190–201.
(51) Lu, J. B.; Yang, H. X.; Li, Z. A.; Ma, C.; Shi, H. L.; Zeng, L. J.; Li, J. Q. Phase Separation, Cation Ordering and Nano-Structural Complexities in $Nd_{2/3-x}Li_{3x}TiO_3$ with x=0.14. *J. Solid State Chem.* **2008**, *181*, 3194–3199.
(52) Bowman, H. L. On the Structure of Perovskite from the Burgumer Alp, Pfitschthal, Tyrol. *Miner. Mag* **1908**, *15*, 156–176.
(53) Kay, H. F.; Bailey, P. C. Structure and Properties of $CaTiO_3$. *Acta Crystallogr.* **1957**, *10*, 219–226.
(54) White, T. J.; Segall, R. L.; Barry, J. C.; Hutchison, J. L. Twin Boundaries in Perovskite. *Acta Crystallogr. B* **1985**, *41*, 93–98.
(55) Fourquet, J. L.; Duroy, H.; Crosnier-Lopez, M. P. Structural and Microstructural Studies of the Series $La_{2/3-x}Li_{3x}\square_{1/3-2x}TiO_3$. *J. Solid State Chem.* **1996**, *127*, 283–294.
(56) Azough, F.; Wang, W.; Freer, R. The Crystal Structure of $LaAlO_3$ -Stabilized $La_{2/3}TiO_3$ Ceramics: An HRTEM Investigation. *J. Am. Ceram. Soc.* **2009**, *92*, 2093–2098.
(57) Azough, F.; Freer, R.; Schaffer, B. Direct Observation of A-Site Vacancies and a Twin Boundary Structure in $La_{2/3}TiO_3$-Based Ceramics Using HAADF/STEM. *J. Am. Ceram. Soc.* **2010**, *93*, 1237–1240.
(58) Browning, N. D.; Pennycook, S. J.; Chisholm, M. F.; McGibbon, M. M.; McGibbon, A. J. Observation of Structural Units at Symmetric [001] Tilt Boundaries in $SrTiO_3$. *Interface Sci.* **1995**, *2*, 397–423.
(59) Browning, N. D.; Pennycook, S. J. Direct Experimental Determination of the Atomic Structure at Internal Interfaces. *J. Phys. Appl. Phys.* **1996**, *29*, 1779.
(60) Van Aert, S.; Turner, S.; Delville, R.; Schryvers, D.; Van Tendeloo, G.; Salje, E. K. H. Direct Observation of Ferrielectricity at Ferroelastic Domain Boundaries in $CaTiO_3$ by Electron Microscopy. *Adv. Mater.* **2012**, *24*, 523–527.

For Table of Contents Only

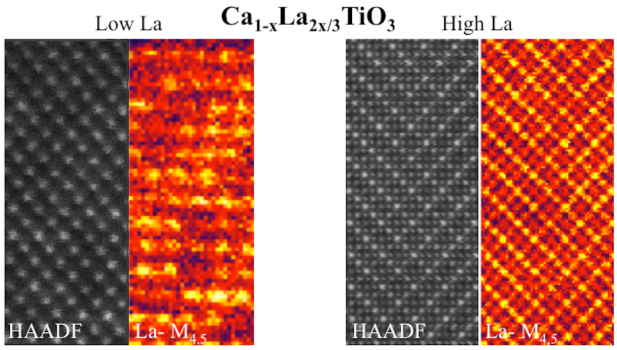

A detailed STEM/EELS characterisation of the $Ca_{(1-x)}La_{2x/3}TiO_3$ perovskite system is presented in two cases of La-lean and La-rich compositions. In La-lean perovskite, tilt boundaries only evident in the BF image, requiring quantitative displacement analysis based on the HAADF signal for correct identification, were observed. In the La-rich case, evidence is shown that a highly ordered phase coexists alongside the single perovskite phase. Distortions in O/Ti lattice explain deviation from reported tilt system in La-rich CLTO.